



Constructing a novel ternary Fe(III)/graphene/g-C₃N₄ composite photocatalyst with enhanced visible-light driven photocatalytic activity via interfacial charge transfer effect

Qiong Liu, Yarong Guo, Zhihong Chen, Zhengguo Zhang, Xiaoming Fang*

Key Laboratory of Enhanced Heat Transfer and Energy Conservation, The Ministry of Education, School of Chemistry and Chemical Engineering, South China University of Technology, Guangzhou 510640, China

ARTICLE INFO

Article history:

Received 22 August 2015
Received in revised form 21 October 2015
Accepted 30 October 2015
Available online 3 November 2015

Keywords:

Photocatalysis
Visible-light driven photocatalyst
g-C₃N₄
Interfacial charge transfer

ABSTRACT

Interfacial charge transfer effect (IFCT) was introduced into g-C₃N₄ by grafting Fe(III) species on its surface via a simple impregnation method. It has been shown that the obtained Fe(III)-grafted g-C₃N₄ photocatalyst exhibited enhanced visible-light absorption, reduced charge recombination and improved photocatalytic activity as compared with those of g-C₃N₄, due to the interfacial charge transfer between the Fe(III) species and g-C₃N₄. Furthermore, a novel ternary Fe(III)/graphene/g-C₃N₄ photocatalyst was successfully constructed by integrating graphene into the binary Fe(III)/g-C₃N₄ composite as the electron mediator. It has been found that the introduction of graphene made the Fe species show well distribution, smaller size and relatively high content in the ternary photocatalyst as compared with those in the binary one, revealing a synergistic effect between the Fe(III) species and graphene existed in the ternary photocatalyst. Consequently, the photocatalytic activity of the ternary Fe(III)/graphene/g-C₃N₄ photocatalyst was superior to that of the binary one, originating from its stronger visible-light absorption and more reduced charge combination. The ternary composite that consists of transition metal, graphene and g-C₃N₄ represents a new kind of high-efficiency visible-light-driven photocatalysts for water disinfection.

© 2015 Elsevier B.V. All rights reserved.

1. Introduction

Semiconductor-based photocatalysis is a potential strategy to solve the problems concerning energy crisis and environmental contamination through photocatalytic water splitting to produce hydrogen and degradation of organic pollutants into carbon dioxide and H₂O [1]. Photocatalysts with high activity and good stability are essential for putting the semiconductor-based photocatalysis technology into practical applications. However, the most widely used and representative semiconductor photocatalysts can only respond to UV irradiation, which greatly limits their practical applications under solar light [2]. Therefore, developing novel visible-light response photocatalysts with high quantum efficiency has become a hot topic in the photocatalysis field.

Graphitic carbon nitride (g-C₃N₄), a metal-free polymeric semiconductor, possesses a two-dimensional layered structure, a relatively narrow band gap (~2.7 eV), high chemical stability, and suitable valence and conduction band potentials for photo-

catalytic splitting of water to generate hydrogen and oxygen [3]. These unique properties make g-C₃N₄ a promising visible-light active photocatalyst for use in the production of hydrogen and the degradation of organic pollutants [4]. However, it has been found that g-C₃N₄ suffers from narrow visible-light response range, fast charge recombination, slow charge transport, and low specific surface area [5], thereby exhibiting low photocatalytic activity. To overcome these drawbacks inherent in g-C₃N₄, various strategies have been explored, including doping of metal and/or nonmetal ions [6], forming of heterojunctions [7], copolymerization with organic molecules [8], combination with other semiconductors [9] or carbon materials [10], and fabrication of g-C₃N₄ microporous [11] and hierarchical [12] structures. Although the photocatalytic activity of g-C₃N₄ has been improved by the above strategies to varying degrees, the obtained g-C₃N₄-based photocatalysts still cannot satisfy the needs of actual applications with respect to visible-light activity and stability.

Interfacial charge transfer (IFCT) between the discrete energy levels of molecular species and the continuous ones of solids has been proven to be a powerful strategy to enhance the visible-light activity of semiconductor photocatalysts [13]. Irie et al. [14] prepared efficient visible-light sensitive TiO₂ based photocatalysts by

* Corresponding author. Fax: +86 20 87113870.
E-mail address: cexmfang@scut.edu.cn (X. Fang).

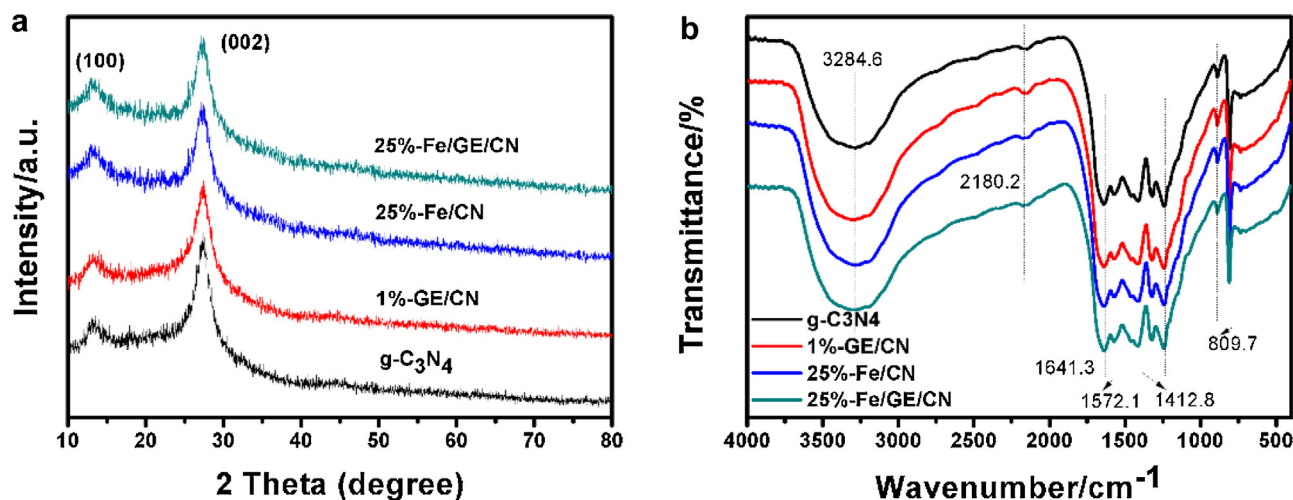


Fig. 1. XRD patterns (a) and FT-IR spectra (b) of g-C₃N₄, 1%-GE/CN, 25%-Fe/CN and 25%-Fe/GE/CN.

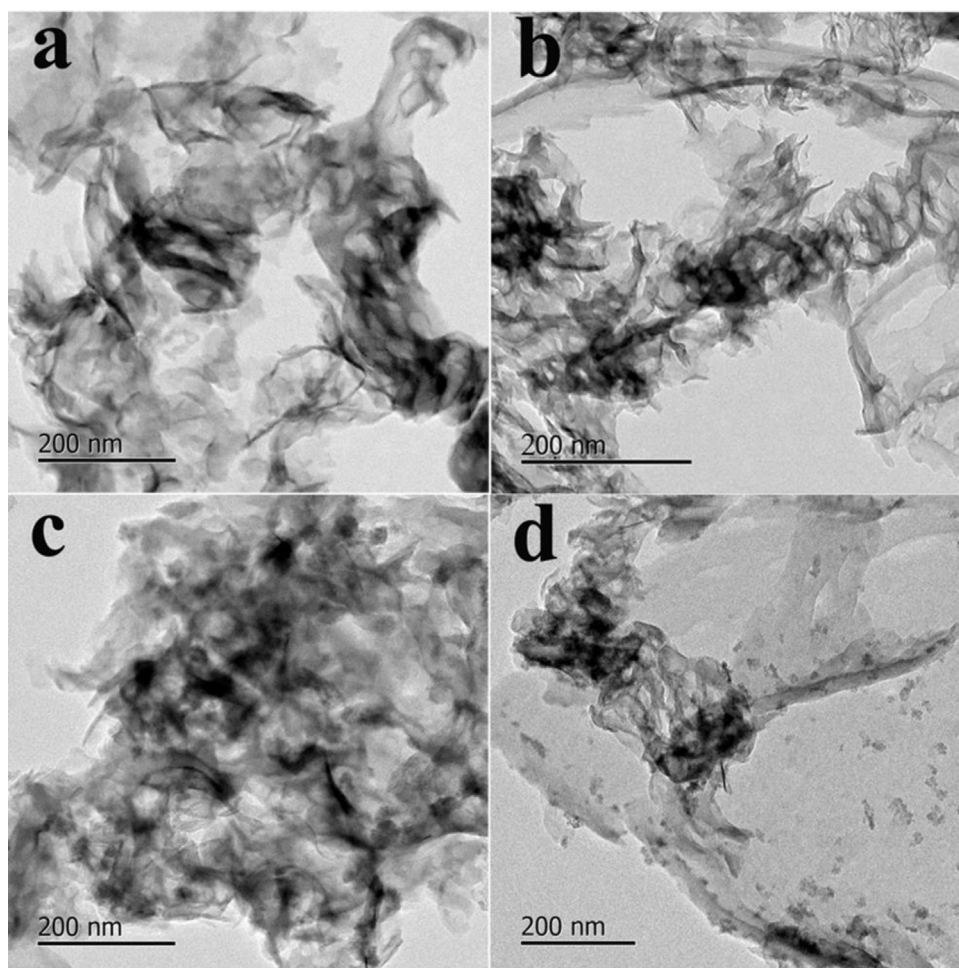


Fig. 2. TEM images of g-C₃N₄ (a), 1%-GE/CN(b), 25%-Fe/CN(c) and 25%-Fe/GE/CN(d).

grafting Cu(II) or Fe(III) ions on the surface of TiO₂ via a facile impregnation method. And he found that the enhancement in visible-light driven photocatalytic activity of the Cu(II)- or Fe(III)-grafted TiO₂ photocatalysts was attributed to the fact that a portion of photo-generated electrons directly transferred from the valence band of TiO₂ to the Cu(II) or Fe(III) species that served as the active site for exerting the multi-electron reduction. In addition, Yu et al.

[15] also reported that the photocatalytic activity of Ag₃PO₄ has been increased by grafting the Fe(III) species on the surface of Ag₃PO₄ by the impregnation method, originating from the IFCT between the Fe(III) and Ag₃PO₄, implying the possibility of others semiconductor-based composites via IFCT. Very recently, Wang et al. [16] reported that g-C₃N₄ possessed so-called “nitrogen pots” which were filled with six long-pair electrons of nitrogen, they were

feasible ideal sites for metal inclusion. So the transition metal doped or complexation modified with g-C₃N₄ was available. And there were reported that the transition metal species such as iron doped g-C₃N₄ [6c], ferrocene [17] or cobalt compounds [18] incorporation with g-C₃N₄ showed the enhanced photocatalytic activity. It was demonstrated the inclusion of the transition metal into g-C₃N₄ was an effective way to increase the photocatalytic performance. While to the best of our knowledge, the inclusion of transition metal into g-C₃N₄ via the IFCT for improving its photocatalytic activity has not been reported yet.

In the current work, the IFCT was first introduced into g-C₃N₄ by grafting Fe(III) species on its surface via a simple impregnation method. It is shown that the obtained Fe(III)-grafted g-C₃N₄ photocatalyst exhibits enhanced visible-light absorption, reduced charge recombination and improved photocatalytic activity as compared with g-C₃N₄, owing to the interfacial charge transfer between the Fe(III) species and g-C₃N₄. Furthermore, aiming at further increasing the photocatalytic activity of the binary Fe(III)-grafted g-C₃N₄, a novel ternary Fe(III)/graphene/g-C₃N₄ composite photocatalyst was constructed by integrating graphene into the binary one. It is revealed that a synergistic effect between the Fe(III) species and graphene [19] existed in the ternary catalyst, result in its stronger visible-light absorption, less charge combination, and higher photocatalytic activity as compared with those of the binary one. This work sheds light on a new kind of ternary photocatalysts with high visible-light-driven activity for water disinfection, which consists of transition metal, graphene and g-C₃N₄.

2. Experimental

2.1. Materials

Urea, iron nitrate (Fe(NO₃)₃·9H₂O), 5,5-dimethyl-1-pyrroline-N-oxide (DMPO) and

2,2,6,6-tetramethylpiperidinyloxy (TEMPO) were purchased from Sigma-Aldrich Chemical Co., Graphene dispersion liquid was purchased from Nanjing XFNANO Materials Tech Co., Ltd., and used without further purification.

2.2. Preparation of photocatalysts

2.2.1. Preparation of g-C₃N₄

g-C₃N₄ was prepared from urea [20]. Briefly, 10 g of urea placed in a crucible with a cover was heated at 80 °C for 5 h, followed by calcining at 550 °C for 3 h in a muffle furnace. After natural cooling to room temperature, the obtained sample was taken out and milled into powder.

2.2.2. Preparation of Fe(III)/g-C₃N₄

The Fe(III)-grafted g-C₃N₄ photocatalyst was prepared by the impregnation method. Specifically, 0.2 g of g-C₃N₄ was added into 100 ml of a Fe(NO₃)₃ aqueous solution (6 mM). After stirring for 0.5 h, the mixture was ultrasonically dispersed for 0.5 h, followed by stirring at 60 °C for 8 h. The final product was collected and dried at 60 °C for 6 h. Since the nominal mole fraction of Fe/g-C₃N₄ in this sample was calculated to be 25%, it was named as 25%-Fe/CN.

2.2.3. Preparation of graphene/g-C₃N₄

0.3 ml of a graphene dispersion (1 mg/ml) was added into 100 ml of distilled water followed by stirring for 0.5 h and added some HCl under stirring to adjust the pH 2. Then, 0.2 g g-C₃N₄ was added to the obtained dispersion. The mixture solution was stirred for 0.5 h and then ultrasonically dispersed for 0.5 h. After being collected by centrifuge, washed and dried, the sample was obtained

and denoted as 1%-GE/CN, in which the nominal mole fraction of graphene to g-C₃N₄ was calculated to be 1%.

2.2.4. Preparation of Fe(III)/graphene/g-C₃N₄

In a typical process, 0.3 ml of graphene dispersion (1 mg/ml) was added to 100 ml of a Fe(NO₃)₃·9H₂O aqueous solution (6 mM) followed by stirring for 0.5 h and adjusted the pH 2. Then, 0.2 g g-C₃N₄ was added to the mixed solution. After dispersing for 0.5 h using an Ultrasonic Cell Crusher, the obtained solution was stirred at 60 °C for 8 h. The final product was collected and dried at 60 °C for 6 h. Since the nominal mole fraction of Fe to g-C₃N₄ in this sample was 25%, it was named as 25%-Fe/GE/CN. Moreover, 5%-, 10%-, 15%-, and 20%-Fe/GE/CN samples were prepared by changing the amount of Fe(NO₃)₃ via the same process, in which the nominal mole fraction of graphene to g-C₃N₄ was fixed at 1%. In addition, in order to investigate the effect of the charging sequence on the properties and activity of the ternary photocatalyst, 25%-Fe/CN/GE and CN/GE/Fe-25% were also prepared. 25%-Fe/CN/GE was obtained from mixing the Fe(NO₃)₃ solution with g-C₃N₄ followed by adding graphene, while CN/GE/Fe-25% was prepared by mixing g-C₃N₄ with graphene followed by adding the Fe(NO₃)₃ solution.

2.2.5. Preparation of Fe(III)/graphene

0.3 ml of a graphene dispersion (1 mg/ml) was added into 50 ml 0.05 g Fe(NO₃)₃ solution, the mixture was ultrasonically dispersed for 0.5 h, followed by seal stirring at 60 °C for 8 h. And then direct used for degradation test of MO without further steps.

2.3. Characterization

The structural properties of the samples were examined by powder X-ray diffraction (XRD, D/max-III A, Rigaku, Japan) measurements which using Cu K α radiation at a scanning rate of 0.02 degree/s in the 2 θ range from 10° to 80°. The morphologies and microstructures of the samples were observed by a transmission electron microscope (TEM, JEM2100F, JEOL, Japan). Elemental analysis of iron species was performed using an inductively coupled plasma optical emission spectrometer (Varian ICP-OES 720, USA). UV/VIS/NIR diffuse reflectance spectra of the samples were detected by a Lambda 950 UV/VIS/NIR spectrophotometer (Perkin-Elmer, America) and BaSO₄ was used as a reflectance standard. Photoluminescence (PL) spectra of the photocatalysts were recorded on an F-4600 spectrometer (Hitachi, Japan) with an excitation wavelength of 375 nm. X-ray photoelectron spectroscopy (XPS) measurements were conducted on a THETA Prode spectrometer (PHI 5300 ESCA, Ulvac-Phi, Japan) for identifying chemical states of the samples, and the spectra were calibrated to the C 1s peak at 284.8 eV. Electron spin resonance (ESR) signals were obtained using a Bruker model A300 electron paramagnetic resonance spectrometer equipped with a 300 W Xe lamp (420 nm filter) as visible light source. The infrared absorption spectra were investigated using a Fourier transform infrared (FT-IR) spectrophotometer (Vector 33, Bruker, Germany) in the wavenumber range from 400 to 4000 cm⁻¹. The specific surface area (BET) and pore volume were collected at a Micromeritics ASAP 2460 apparatus and porosity analyzer. Atomic Fluorescence spectrometer (AFS-9130, Beijing Titan) was used to check the leakage of the iron species in reaction system after ending irradiation.

2.4. Evaluation of photocatalytic activity

The degradation of methylene orange (MO) aqueous solution was carried out for the evaluation of the photocatalytic activities of the samples under visible light irradiation. In a typical process, 0.05 g of the as-prepared sample was added into 100 ml MO solution (10 mg/L). Before irradiation, the solution was stirred for

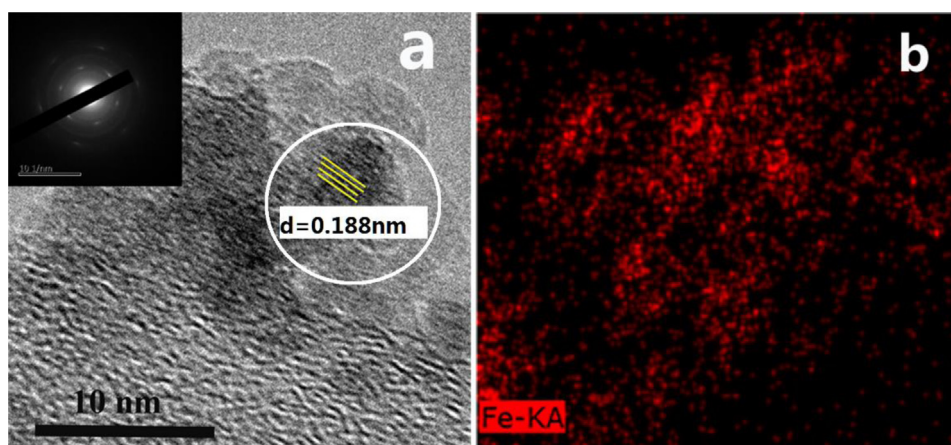


Fig. 3. HRTEM images and the selected area electron pattern (SAED) of 25%-Fe/GE/CN (a) and the element mapping analysis of Fe over 25%-Fe/GE/CN (b).

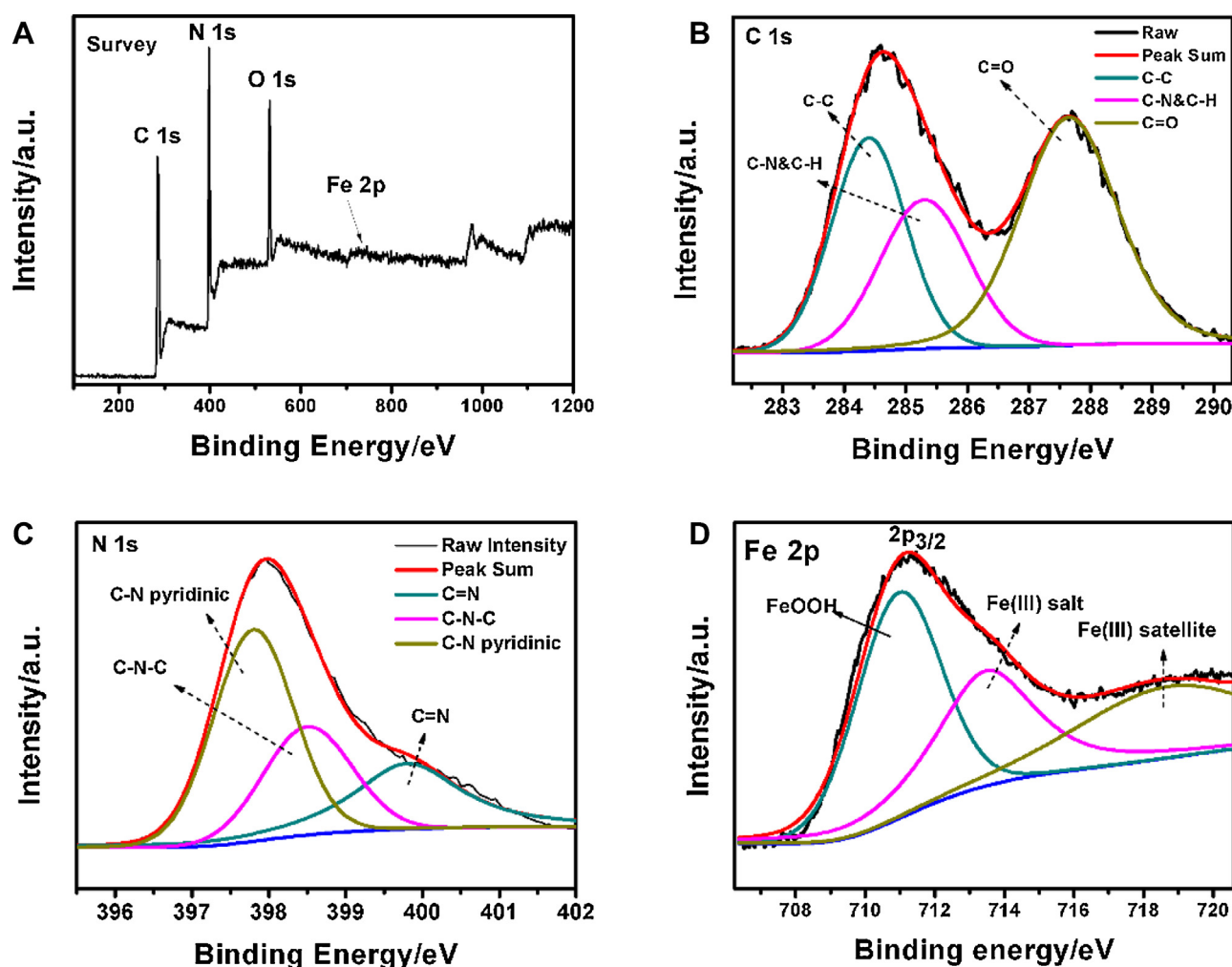


Fig. 4. XPS spectra of the fresh 25%-Fe/GE/CN sample: Survey (A), C1s (B), N1s (C), and Fe 2p (D).

30 min in a darkroom to ensure the adsorption–desorption equilibrium. Then, a 300 W Xe lamp (Beijing Perfect Light Technology Co., China) with a 420 nm cutoff filter was used as the light source. At every 10 min interval, 3 ml of the suspension solution was removed and centrifuged to obtain the clear MO solution. The concentration was measured by a UV–vis spectrophotometer (UV-2050, Shimadzu, Japan) in the range from 220 nm to 800 nm. The degradation of another model pollutant phenol (10 mg/L) was conducted under

identical condition with MO. Total organic carbon (TOC) of the MO solutions was recorded by High Temperature TOC/TNb Analyzer (Liqui TOC II, Elementar, Germany). Liquid chromatography–mass spectrometry (LC–MS) was exploited to identify the products of MO under photoexcitation times. The LC–MS was equipped with a Zorbax C18 column ($150 \times 4.6 \text{ mm i.d.}, 5 \mu\text{m}$) and coupled on-line with an LC/MSD Trap XCT ion-trap mass spectrometer (Agilent Technologies, America).

For the detection of the active species during the photocatalytic reaction, benzoquinone (BQ), ammonium oxalate (AO), and isopropanol (IPA) were added into the MO suspension solution containing the 25%-Fe/GE/CN composites photocatalyst to trap superoxide radicals ($O_2^{\bullet-}$), holes (h^+), and hydroxyl radicals ($\bullet OH$), respectively. Moreover, N_2 purge and NaN_3 were also added into the photocatalytic reactions system, respectively. Electron spin resonance (ESR) signals of radicals trapped by 5,5-dimethyl-1-pyrroline-*N*-oxide (DMPO) and 2,2,6,6-tetramethylpiperidinyloxyl (TEMPO).

2.5. Electrochemical measurements

Typically, the working electrode was prepared by the doctor-blading methods as follows. 0.1 g catalyst and 0.01 g ethyl cellulose were grinded into fine slurries in ethanol and coated onto FTO glass sheet, then dried at 120 °C for 1 h. An electrochemical analyzer (CorrTest CS350) with a standard three-electrode system was used to perform the electrochemical measurements and Pt wire and Ag/AgCl were used as the counter electrode and reference electrode, respectively. 0.25 M Na_2S /0.35 M Na_2SO_3 aqueous solution was used as the supporting electrolyte in this system. A 300 W Xe lamp with a UV-cutoff filter ($\lambda > 420$ nm) served as a light source and the periodic ON/OFF photocurrent response with a 1 cm² area of the work electrode were carried out at a constant potential of +0.5 V vs. Ag/AgCl electrode.

3. Results and discussion

3.1. Structure and morphology

Fig. 1a displayed the XRD patterns of g- C_3N_4 , 1%-GE/CN, 25%-Fe/CN and 25%-Fe/GE/CN. There presented two distinct diffraction peaks at 13.2° and 27.5° in the XRD patterns of all the samples, which could be well indexed to graphitic C_3N_4 (JCPDS Card No. 87-1526). The low angle diffraction peak at 13.2° accorded with the repeated tri-s-thiazine units (100), and the other stronger one at 27.5° was derived from the interlayer (002) diffraction of graphitic like structures [3a]. There was no significant difference in diffraction pattern among g- C_3N_4 , 1%-GE/CN, 25%-Fe/CN and 25%-Fe/GE/CN, suggesting that the crystal structure and crystallization of g- C_3N_4 were not affected by the combination with graphene and the deposition of Fe(III) species. The absence of the diffraction peaks for graphene and Fe species might be attributed to the low content of graphene in the composite photocatalysts and the poor crystallinity of the Fe(III) species formed under the mild conditions. It was suggested that the Fe(III) species were just grafted on g- C_3N_4 , not embedded into its interlayers.

FT-IR was carried out to elucidate the difference in chemical structure among g- C_3N_4 , 1%-GE/CN, 25%-Fe/CN and 25%-Fe/GE/CN, as was shown in Fig. 1b. In the FT-IR spectrum of g- C_3N_4 , the broadened band at 3284 cm⁻¹ was ascribed to the N–H stretching vibration of g- C_3N_4 [21]. The several strong peaks ranged from 1800 to 1400 cm⁻¹ are assigned to C=N and C–N heterocycles skeletal vibration of the aromatic ring. The bands at 1320 and 1241 cm⁻¹ represented the stretching vibrations of C–NH–C bridges. And the sharp peak at 809 cm⁻¹ corresponded to the C–N stretching vibration of the characteristic mode of the triazine cycles. Note that a small signal at 2180 cm⁻¹ assigned to the appearance of C≡N and N=C=N, it might come from the little fragment of diazo groups adhered to the surface, but actually these may do not affect the formation of this body organic network structure. While, for the 1%-GE/CN, 25%-Fe/CN and 25%-Fe/GE/CN composites, no distinct changes were observed in comparison with g- C_3N_4 , manifesting

that the introduction of graphene and Fe(III) species didn't change the chemical structure of g- C_3N_4 .

Fig. 2 displayed the TEM images of g- C_3N_4 , 1%-GE/CN, 25%-Fe/CN and 25%-Fe/GE/CN. The bare g- C_3N_4 sample consisted of thin nanosheets with wrinkles shape, in which several black stripes corresponded to some overlap layers, as was shown in Fig. 2a. For 1%-GE/CN, it can be seen from Fig. 2b that graphene flakes were uniformly covered on the nanosheets of g- C_3N_4 and well interconnect with the nanosheets of g- C_3N_4 , resulting in the intimate interfacial contact between g- C_3N_4 and graphene. The elemental mapping analysis of C and N elements was conducted in Fig. S1 (see Supporting materials), also suggesting the well distribution of graphene flakes over nanosheets of g- C_3N_4 . As was shown in the TEM image of 25%-Fe/CN (Fig. 2c), some black and gray spots (20–50 nm) appear, which corresponded to the Fe(III) clusters attached to the nanosheets of g- C_3N_4 . It was indicated that the Fe(III) clusters were successfully grafted on the nanosheets of g- C_3N_4 via the impregnation method. For the ternary 25%-Fe/GE/CN composite, it was found from Fig. 2d that a lot of Fe(III) clusters were uniformly grafted on both the nanosheets of graphene and g- C_3N_4 , and their sizes were obviously smaller than those of the Fe(III) clusters in the 25%-Fe/CN sample (Fig. 2c). It was suggested that the introduction of graphene resulted in a reduction in size and a more uniform distribution of the Fe(III) clusters, probably owing to the strong electron affinity force and high surface area of graphene [10a].

In order to further clarify the microstructure of the ternary photocatalyst, TEM observation was conducted on 25%-Fe/GE/CN. Fig. 3 displays the HRTEM image and the selected area electron diffraction (SAED) of 25%-Fe/GE/CN, together with the elemental mapping analysis of Fe(III) species. As shown in the HRTEM image (Fig. 3a), the lattice spacing of the Fe species was measured to be about 0.188 nm, corresponding to the (005) plane of FeOOH (JCPDS No. 461315) [22]. Obscure diffraction rings and bright spots were observed in the SAED pattern (inset of Fig. 3a). The indistinct rings suggested the low crystallinity of FeOOH, which agreed with the XRD results. The bright diffraction spots in an hexagonal arrangement were attributed to graphene grains [23], verifying the existence of graphene in the ternary photocatalyst. These results implied that Fe(III) clusters formed by the impregnation method were in the form of amorphous FeOOH-like clusters, and some of them grafted on the graphene nanosheets. The corresponding elemental mapping analysis of Fe (Fig. 3b) indicated a well spatial distribution of the Fe clusters in the ternary 25%-Fe/GE/CN photocatalyst, which could result in more active sites for generating the IFCT between the Fe(III) species and g- C_3N_4 .

Fig. 4 presented the XPS analysis of fresh 25%-Fe/GE/CN sample. The XPS survey spectrum of different elements was shown in Fig. 4A. It was clear that only the C, N, O and Fe elements have been detected on the surface of the ternary composite. The high-resolution C 1s spectrum (Fig. 4B) fitted into several C species with different binding energy, including graphite CC (284.4 eV), C–H&C–N (285.3 eV) and C=O (287.5 eV), which suggesting the successful coupled graphene with g- C_3N_4 . With regard to the N 1s spectrum (Fig. 4C), there exhibited three N states including pyridinic-N (397.8 eV) [24], triazine rings C–N–C (398.5 eV) and tertiary nitrogen N–(C)₃ (399.8 eV) [25], which were the three N units that constituted the basic units of g- C_3N_4 . It was suggested that the framework of g- C_3N_4 was not changed after it has been combined with graphene and the Fe(III) clusters. As shown in Fig. 4D, Fe 2p_{3/2} located at 710.9 eV and 713.4 eV, and the corresponding symmetric peaks of Fe 2p_{1/2} appeared at 723.9 eV and 726.4 eV (Fig. S2, Table S1/S2, Supporting Information), respectively. It was deduced that the binding energy at 710.9 eV belonged to FeOOH [26], and the other peak at 713.4 eV was consistent with the Fe(III) salt, resulting from the excess of Fe(III) ion. While, the

banding energy at 718.7 eV was ascribed to the Fe(III) satellite peak [27]. It was revealed that the Fe(III) ions, derived from the Fe(NO₃)₃ aqueous solution, being not changed into metallic Fe or Fe(II) ion during the preparation of the ternary photocatalyst and existed in the form of FeOOH.

Compared Fe 2p spectrum to 25%-Fe/GE/CN and 25%-Fe/CN in Fig. S2, the binding energy of the several corresponding Fe(III) peaks in 25%-Fe/CN were the same as the 25%-Fe/GE/CN, implying the similar composition of Fe(III) species among two composite. While the peak intensity and relatively theoretical area ratio of FeOOH in 25%-Fe/GE/CN was larger than the other, indicating more FeOOH-like clusters grafted on 25%-Fe/GE/CN composites. These results suggested the introduction of graphene enabled the function of increasing the content of the Fe(III) species in the ternary composite, besides those of reducing the sizes of the Fe clusters and making them well-distributed (Fig. 2). The influences of graphene could be attributed to its strong electron affinity force and high surface area. The N₂ sorption–desorption isotherm and Barrett–Joyner–Halenda (BJH) pore size distributions was carried out, as shown in Fig. S3 and listed in Table S3. The BET area and pore volume of g-C₃N₄ is estimated as 89.681 m²/g and 0.254 cm³/g. While the other samples showed little difference with g-C₃N₄, suggesting the specific surface area did not play an important role in photocatalytic performance.

3.2. Optical properties

Fig. 5A showed the UV–vis–NIR spectrum of g-C₃N₄, 1%-GE/CN, 25%-Fe/CN and 25%-Fe/GE/CN. Compared with g-C₃N₄, 1%-GE/CN showed a similar absorption region in 400–450 nm and no change in band-gap. While exhibited an enhanced visible light intensities toward a longer wavelength region, which was ascribed to intimate interfacial contact between g-C₃N₄ and graphene [28]. For 25%-Fe/CN, they presented much enhanced visible-light absorption and large red shift of absorption edge from 400 to 780 nm, as compared with g-C₃N₄, indicating that the optical absorption property of g-C₃N₄ can be remarkably improved by grafting the Fe(III) clusters on its surface and this similar phenomenon was also observed by several previous reports [14b,29]. Especially, the grafted Fe(III) species on g-C₃N₄ also showed a absorption light intensities in near-infrared region from 780 nm to 1600 nm. It was implied that the IFCT of valence band electrons of g-C₃N₄ to surface-grafted Fe(III) species largely shorten transition distance. Considering the IFCT from the valence band of g-C₃N₄ (1.57 V) to Fe(III)/Fe(II) (0.77 V, vs SHE pH 0) [30], the energy difference was only about 0.8 V. As a consequence, the IFCT among Fe/CN composites possessed light absorption in the near-infrared region. While it need to point out that, according to Creutz et al. reported [13], the IFCT is just a surface phenomenon. The near-infrared light absorption intensities is weak and the absorbed photo number is small, so the relatively low reduction potential (electrons excited among near-infrared region) may do not contributed to the photocatalytic activity. The optical absorption of 25%-Fe/GE/CN were stronger than that of 25%-Fe/CN, revealing that the introduction of graphene further increased the optical absorption property for the ternary composite. The enhancement in optical absorption could be attributed to the synergistic effect between graphene and the Fe(III) species. As revealed from the TEM and XPS characterizations, the introduction of graphene resulted in the well distribution, small size and relatively high content of the Fe(III) species in the ternary composite, thereby leading to the further increase in visible-light absorption.

Fig. 5B showed the PL emission spectra of g-C₃N₄, 1%-GE/CN, 25%-Fe/CN and 25%-Fe/GE/CN. For g-C₃N₄, a strong emission peak appears at around 450 nm, which is attributed to the band-gap emission in the light of its absorption band edge estimated by the

DRS (Fig. 5A). Compared with g-C₃N₄, 1%-GE/CN and 25%-Fe/CN exhibit PL emission peaks with lower intensities, suggesting that the combination with graphene or the grafting of the Fe(III) species played a role in reducing the recombination between electrons and holes. The excellent electrical conductivity property of graphene could facilitate the delivering of the photo-induced carriers to the active sites, resulting in a reduction in charge combination for the composite photocatalysts containing graphene [10a]. The grafting of Fe(III) clusters paves the way for efficient electron transfer from VB of g-C₃N₄ to Fe(III) and effectively consumed photo-induced electrons via interfacial charge transfer and multielectron reduction reaction [29a], thus suppressing the recombination of photo-induced electron–hole pair. Significantly, the PL emission of 25%-Fe/GE/CN was far lower than those of 1%-GE/CN and 25%-Fe/CN, revealing that the charge combination was further reduced for the ternary composite. This quenching effect can be attributed to the well distribution, small size and relatively high content of the Fe(III) clusters in the ternary composite, resulting from the synergistic effect between graphene and the Fe(III) species.

3.3. Photocatalytic activity

The photocatalytic activity of different samples was evaluated by the degradation of MO under visible light irradiation, as displayed in Fig. 6A. Under visible light illumination, pure g-C₃N₄ showed low photocatalytic activity (only 14% MO degradation in 60 min). The combination of graphene at the mole fraction of 1% (1%-GE/CN, optimized) with g-C₃N₄ presented a small increase in photocatalytic activity (about 30% MO degradation in 60 min), owing to the reduction in charge combination, as revealed by the PL spectra (Fig. 5B). Interestingly, the photocatalytic activity of 25%-Fe/CN was obviously higher than that of g-C₃N₄, suggesting that the IFCT generated by the Fe(III) species grafted on g-C₃N₄ played a more effective role in increasing the photocatalytic activity of g-C₃N₄. More significantly, compared with 25%-Fe/CN, 25%-Fe/GE/CN exhibited much higher photocatalytic activity (82% percent removal of MO in 60 min), owing to its stronger visible-light absorption (Fig. 5A) and the much more reduced charge combination (Fig. 5B) in the ternary composite. Besides, Fe/GE almost had no photocatalytic activity on degradation of MO, after reaching adsorption–desorption equilibrium. Note that the photocatalytic decomposition of MO was supposed to follow a pseudo-first-order kinetics reaction. As shown in Fig. 6B, the kinetic constant of 25%-Fe/GE/CN was estimated to be 0.02765 min^{−1}, which was 1.97, 4.82 and 11.28 times those of 25%-Fe/CN (0.01402 min^{−1}), 1%-GE/CN (0.00574 min^{−1}) and g-C₃N₄ (0.00245 min^{−1}). Apparently, 25%-Fe/GE/CN exhibits the highest photocatalytic activity among all these samples, originating from the synergistic effect between graphene and Fe(III) in the ternary composite.

In view of the important role of the Fe(III) species in increasing the photocatalytic activity, the mole ratio of Fe(III) to g-C₃N₄ in the ternary composite has been optimized and is shown in Fig. 6C. It can be seen that the photocatalytic activity enhances with the nominal mole fraction of Fe to g-C₃N₄ increasing from 5% to 25%. However, as the nominal mole fraction is further increased to 30%, a decrease in photocatalytic activity happens. It can be inferred that the increase in mole fraction of the Fe(III) species in the ternary photocatalyst would cause more defects and induce a shielding effect on g-C₃N₄ [6c], thus decreasing its photocatalytic activity. Moreover, we conducted Fenton and Photo-Fenton reaction over 25%-Fe/GE/CN, as showed in Fig. S4. Fenton effect slightly reduced the concentration of MO, while Photo-Fenton effect had a profound impact on degradation of MO, and it was almost able to completely degraded MO in about 30 min. The photodegradation activity of Photo-Fenton reaction was much higher than 25%-Fe/GE/CN.

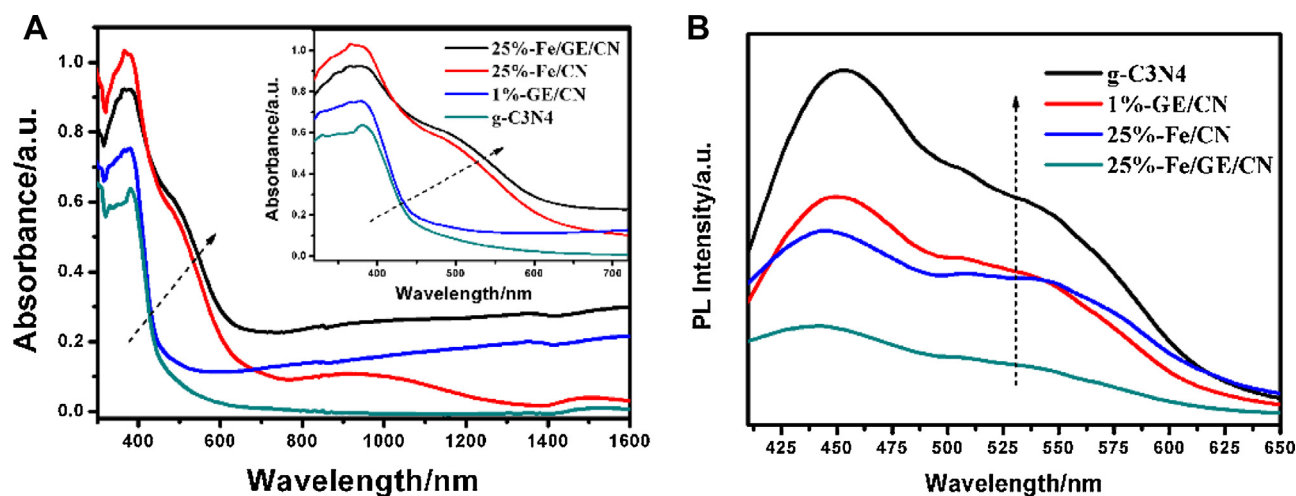


Fig. 5. UV-vis diffuse reflectance spectra (A) and photoluminescence emission spectra (B) of g-C₃N₄, 1%-GE/CN, 25%-Fe/CN and 25%-Fe/GE/CN. The wavelength of excitation light for photoluminescence emission spectra is 375 nm.

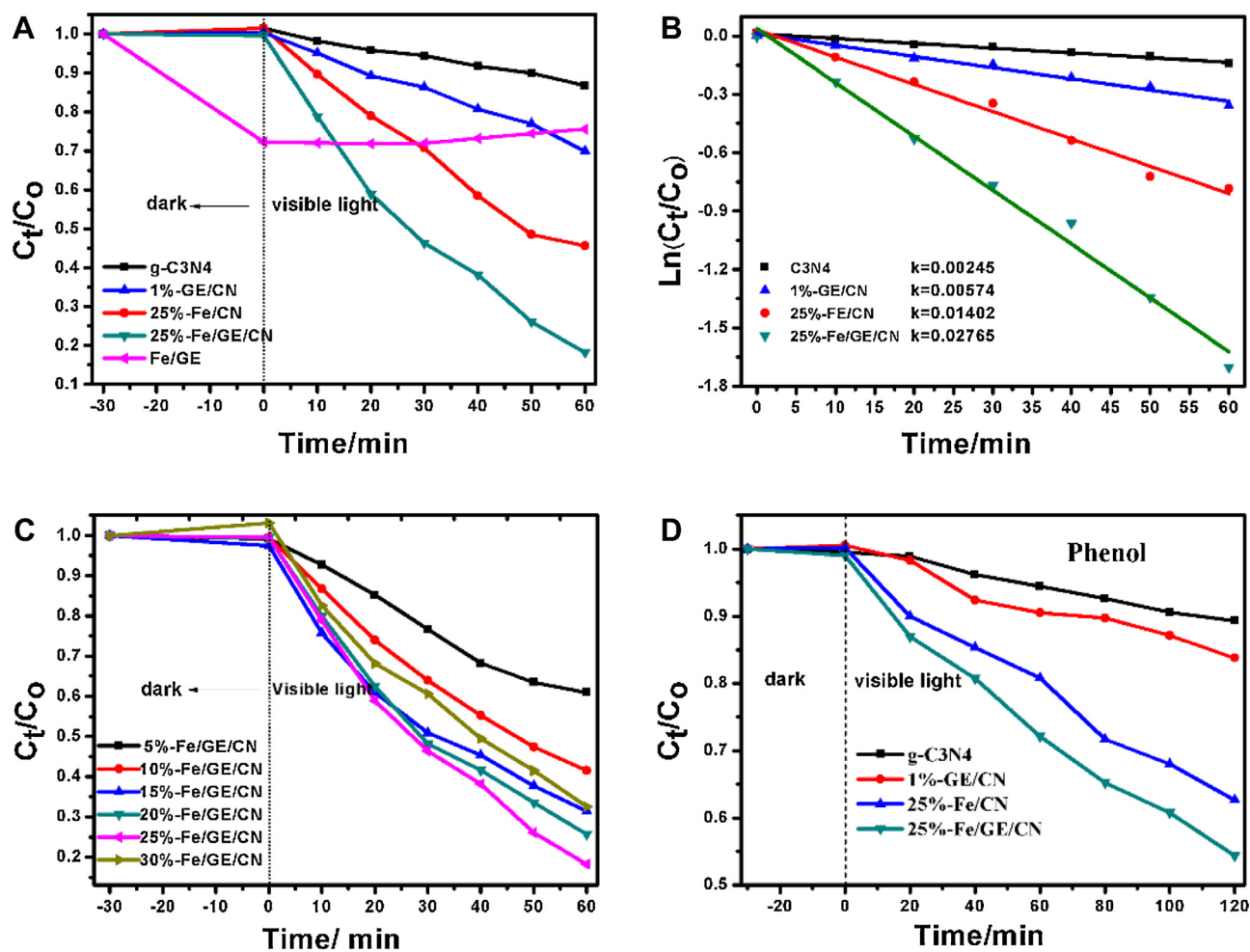


Fig. 6. Photocatalytic activity (A, C) and kinetic constant (B) of the prepared samples on degradation of MO under visible light irradiation ($\lambda > 420$ nm), together with degradation of phenol (D, 10 mg/L) by 25%-Fe/GE/CN.

In addition, phenol, as colorless substances without absorbing visible-light, was used as the second model pollutant to further evaluate the visible light photocatalytic performance of the as-prepared samples under visible light (>420 nm) and the obtained results illustrated in Fig. 6D. It was cleared

that the photodegradation efficiency followed the similar order g-C₃N₄ < 1%-GE/CN < 25%-Fe/CN < 25%-Fe/GE/CN, compared to photodegradation of MO. After 120 min irradiation, about 45.6% percent of phenol was removed over 25%-Fe/GE/CN composites, confirming inherent good visible light photocatalytic activity.

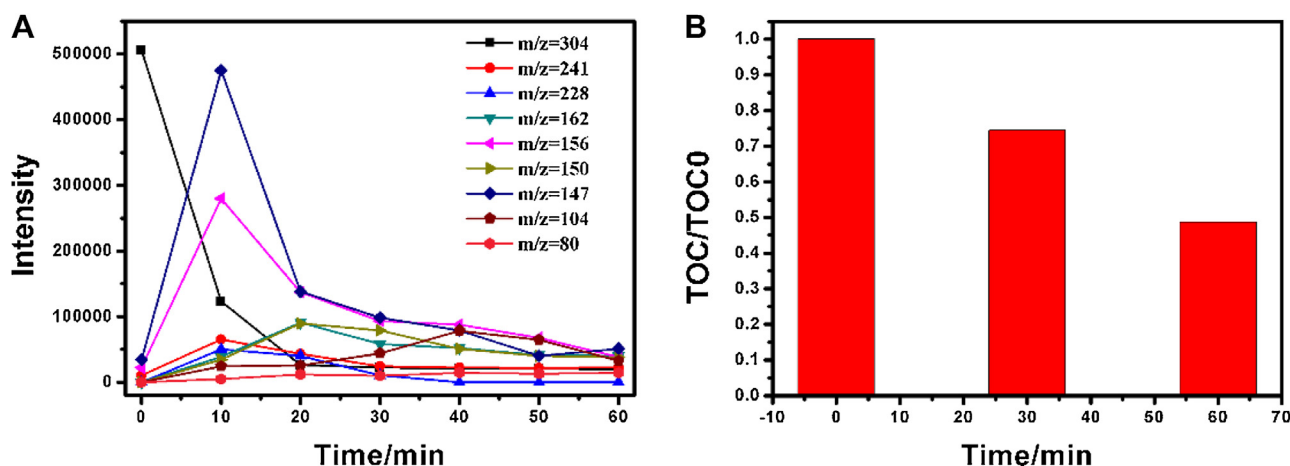


Fig. 7. (A) Mass spectrum intensity variation of the fragment ions peaks appearing under different photoexcitation time among the photodegradation MO and (B) TOC removal of MO over 25%-Fe/GE/CN composites under visible light illumination.

In order to determination the residual dye and intermediates of MO over 25%-Fe/GE/CN, LC-MS was used and Mass spectrum intensity variation of the fragment ions peaks appearing under different photoexcitation time was shown in Fig. 7A. MO molecule presented a signal corresponding to $m/z = 304[M-H]^-$. After irradiation, the peak intensity ($m/z = 304$) decreased rapidly and yielded some fragment ions, such as $m/z = 241[M-H-SO_2]^-$, $m/z = 156[M-H-N_2C_6H_4(CH_3)_2]^-$, $m/z = 147[M-H-C_6H_4SO_3]^-$, etc [31]. Along with irradiation time retention, some degradation intermediate products first increased and then decomposed gradually to smaller molecule fragment, the possible fragment ions of MO was displayed in Fig. S5. Finally, the degradation products exhibited much smaller intensities of the corresponding fragment ions peaks and completely decomposed to inorganic compound to some extent. The total organic carbon (TOC) analysis was also used to assess the mineralization ratio of MO in water over 25%-Fe/GE/CN under visible-light illumination. As illustrated in Fig. 7B, the removal of TOC was about 51.2% after 60 min reaction. It is meant after photodegradation, about 51.2% organic carbon over MO is transformed into inorganic carbon (CO_2). Considering the carbon balance, 10 ppm (10 mg/L) MO will produce about 71.7 ppm CO_2 . Together with LC-MS results (Fig. 7A), it is verified that MO is indeed photocatalytic degraded by the ternary composite, rather than just decolorized by the light irradiation.

To give further evidence to confirm the synergistic effect of Fe(III) and graphene on g-C₃N₄, photoelectrochemical response was carried out, as shown in Fig. 8A. It could be seen that 25%-Fe/GE/CN composite displayed the highest photocurrent intensity. The increase of photocurrent implied a more efficient transportation of photoinduced carriers and the retarded electron/hole recombination. Moreover, it was clear that the transient current of the samples switch reversibly and reproducibly during repeated ON/OFF illumination cycles, indicating both materials exhibit good photophysical stability and this was closely related to the photocatalytic stability. The stability of the ternary 25%-Fe/GE/CN photocatalyst was evaluated by recycling the photocatalytic degradation of MO under visible light irradiation, as displayed in Fig. 8B. The photocatalytic activity of 25%-Fe/GE/CN did not exhibit an obvious decline after five cycling runs, showing nearly 75% degradation of MO in 60 min. A comparison in crystal structure between the fresh and the used 25%-Fe/GE/CN samples was conducted in Fig. S6. No distinct change is found for the ternary photocatalyst after experiencing five cycling runs. Additionally, compared of Fe elemental analysis of the fresh and used 25%-Fe/GE/CN were also performed also performed by ICP-OES, the former weight fraction of Fe rela-

tive to g-C₃N₄ was 0.1991% and the latter was 0.1986%. The weight proportions of the used sample was close to those of the fresh sample and no leakage of the iron species was detected by atomic fluorescence spectrometer after ending irradiation, implying the good stability of 25%-Fe/GE/CN. The good stability of the ternary 25%-Fe/GE/CN composite photocatalyst could be ascribed to the dynamic equilibrium of Fe(III)/Fe(II) under the visible light radiation. On one hand, a Fe(III) species could trap one photogenerated electron and transfers into a Fe(II) species [22]. On the other hand, the formed Fe(II) species is unstable and easily oxidized to Fe(III) by oxygen under ambient condition. As a result, the Fe(III) species can be regenerated, thus making the ternary photocatalyst keep stable.

Together with the above discussed, it's should be noted that Fe(III) ions are not inserted into g-C₃N₄ lattice, however, are grafted onto the surface with the form of amorphous FeOOH-like clusters. The pH adjustment when prepared samples is required, just as Yu et al. reported [14c], as Fe(III) ions in aqueous solution is unstable and easily hydrolysis to form Fe_2O_3 particles which are detrimental to photocatalytic activity. While at acid preparation condition (pH 2), the formation of Fe_2O_3 particles may be retarded. And the photocatalytic activity on degradation of MO with control preparation condition (pH 2, pH 7) of 25%-Fe-GE-CN was conducted, 82% removal percent MO (pH 2) is larger than 70% removal (pH 7) in Fig. S7. Also, in a high temperature, Fe(III) ions prone to form into Fe_2O_3 particles, so the preparation temperature is also needed to control.

3.4. Photocatalytic mechanism

To elucidate the photocatalytic mechanism of the 25%-Fe/GE/CN composite, several main reactive species on the degradation of MO was examined by the radical scavenger experiments in the photocatalytic oxidation (PCO) process, as shown in Fig. 9. Benzoquinone (BQ), ammonium oxalate (AO) and isopropanol (IPA) were used as the radical scavengers for $O_2^{\bullet-}$, h^+ and $\cdot OH$ [32], respectively. The addition of IPA just slightly retarded the photocatalytic oxidation of MO, manifesting that $\cdot OH$ is a minor reactive species in the process. The reason for this is that the valence band position of g-C₃N₄ (1.57 eV vs. NHE) is less than that of $\cdot OH/OH^-$ (1.99 eV vs. NHE) [9b]. Note that the $\cdot OH$ is originated from the reaction of dissolved O_2 with the photo induced electron [33]. The addition of BQ used as an efficient trapper of $O_2^{\bullet-}$, inhibited the degradation of MO almost completely. This result indicates that $O_2^{\bullet-}$ radical is the primary oxidation species in this photocatalytic system. The generation of active species $O_2^{\bullet-}$ was confirmed by an ESR spin trap technique

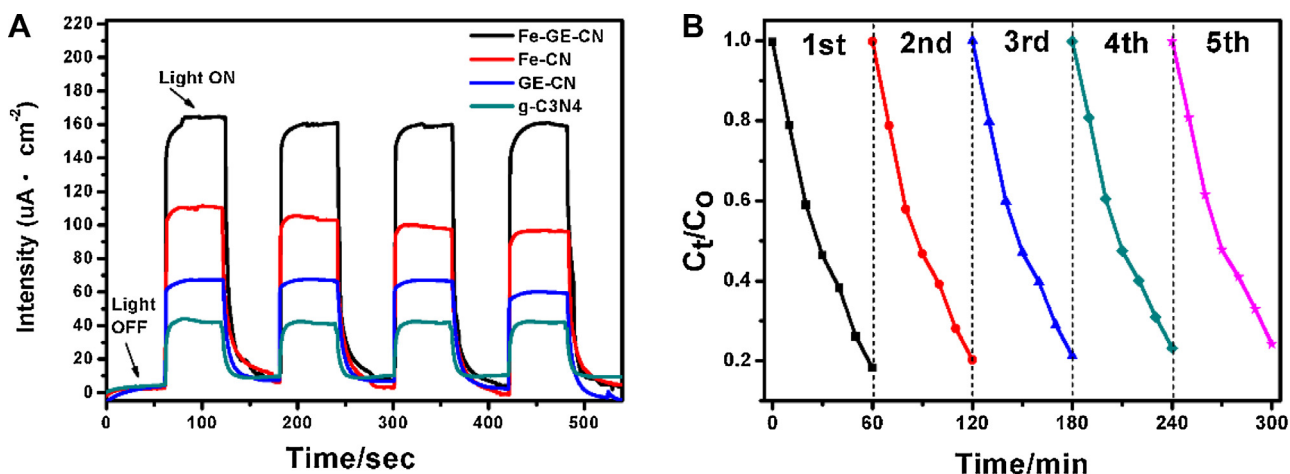


Fig. 8. (A) The transient response of g-C₃N₄, 1%-GE/CN, 25%-Fe/CN and 25%-Fe/GE/CN composites in 0.25 M Na₂S/0.35 M Na₂SO₃ electrolyte under visible light illumination ($\lambda > 420$ nm) at 0.5 V vs. Ag/AgCl electrode and (B) five cycle runs of 25%-Fe/GE/CN for the photodegradation of MO under visible light irradiation ($\lambda > 420$ nm).

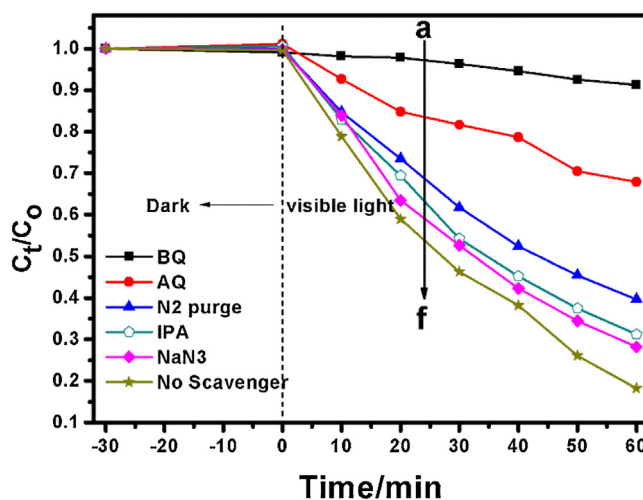


Fig. 9. Kinetic curves of the 25%-Fe/GE/CN composite on the degradation of MO in presence of different radical scavengers under visible light irradiation ($\lambda > 420$ nm) (a) 10 mM BQ; (b) 10 mM AQ; (c) N₂ purge; (d) 10 mM IPA; (e) 10 mM NaN₃; (f) no scavenger addition.

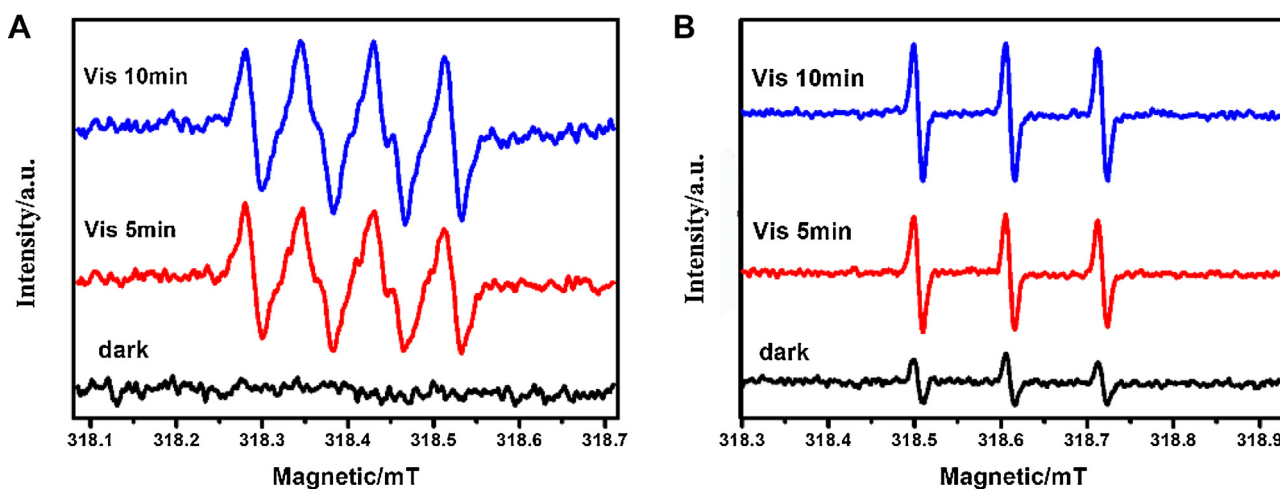
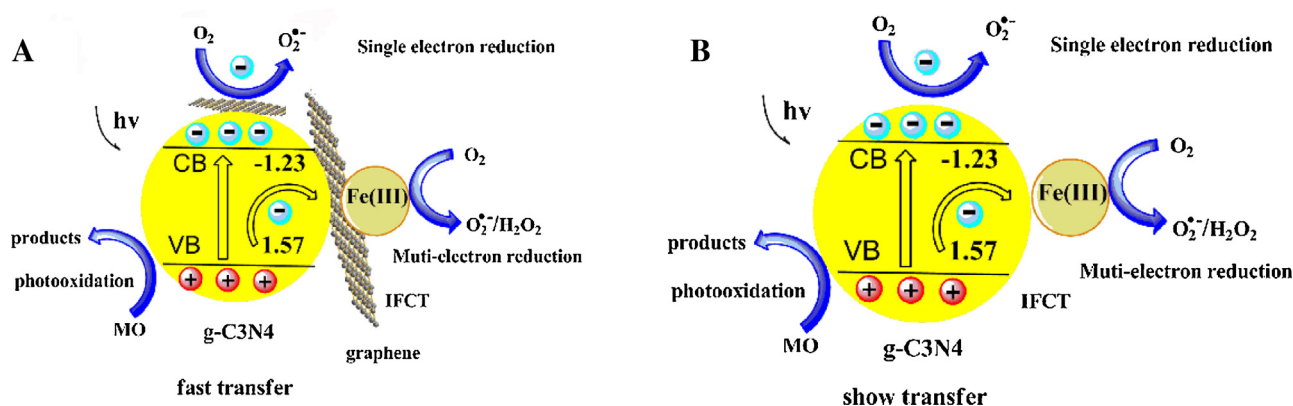


Fig. 10. ESR spectra of DMPO/O₂^{•-} (A) and TEMPO/¹O₂ (B) adducts over the systems of 25%-Fe-GE-CN in water solution before and after 5 min, 10 min visible light irradiation ($\lambda > 420$ nm).



Scheme 1. Schematic illustration of hole-electron separation and transfer process for the 25%-Fe/GE/CN (A) and 25%-Fe/CN (B) photocatalysts under visible light irradiation ($\lambda > 420$ nm).

with DMPO. Typically, 5,5-dimethyl-1-pyrroline-*N*-oxide (DMPO) serves as a radical scavenger of stable DMPO/ $O_2^{\bullet-}$ or DMPO/ $\bullet OH$ species. Under visible light irradiation, it clearly appeared a four-line spectrum with the relative intensities of 1:1:1:1 in Fig. 10A, which was considered to be the characteristic spectrum for the DMPO/ $O_2^{\bullet-}$ adduct [33–34]. While, no obvious ESR signals were observed in the dark time. Besides, no DMPO/ $\bullet OH$ species signals can be found neither darkness nor visible light irradiation. This was consistent with the results that $O_2^{\bullet-}$ was major oxidation active species.

Meanwhile, as the dissolved O_2 in the solution was able to react with photoexcited electrons to form $O_2^{\bullet-}$ active species [9b], it was observed that nearly 60.4% of MO was degraded when N_2 purge was conducted to serve as an $O_2^{\bullet-}$ radical scavengers to suppress the generation of $O_2^{\bullet-}$. While, in the case of the presence of AO (a trapper of h^+), the degradation rate of MO was also significant inhibited but not led to complete suppression of the reaction, only 33% of MO was degraded after 60 min irradiation. Normally, when concerned to C_3N_4 based materials, the trap of h^+ hardly influenced the photocatalytic activity, as the recombination of photo induce carriers [9b]. So it is interesting to find that h^+ plays a significant role on this PCO process, assumed that the visible light initiate interfacial charge transfer (IFCT) from VB of C_3N_4 to Fe(III) and gain the fast separation of electron and hole, leaving holes stay in the VB.

Moreover, the singlet oxygen radical 1O_2 was investigated by ESR with the spin probe, 2,2,6,6-tetramethylpiperidinyloxy (TEMPO). Fig. 10B presented a three-line spectrum with the relative intensity of 1:1:1, referring to the characteristic spectrum of TEMPO/ 1O_2 [34]. When compared to that in the dark, the intensity of TEMPO/ 1O_2 signals was clearly enhanced under the visible light illumination. The generation of singlet oxygen probably results of the oxidation of superoxide radical or transforms from molecule oxygen via energy transfer. The addition of a singlet oxygen quencher, N_3^- , didn't reduce the photocatalytic performance too much, suggesting that 1O_2 was just a minor active species. Therefore, according to the above results, it demonstrates the fact that both $O_2^{\bullet-}$ and h^+ active species are the major oxidation species over the 25%-Fe/GE/CN composite in the process of MO degradation. In addition, MO degradation over the 25%-Fe/GE/CN samples with the different pH value were also conducted, as displayed in Fig. S8. It was found that the degradation efficiency largely increased with reducing pH value. This results further confirmed that O_2 was used as the terminal oxidation reagent. When the moderate $O_2^{\bullet-}$ produced from dissolved O_2 , as $[H^+]$ existed, it would assist $O_2^{\bullet-}$ to react with electron to form H_2O_2 (Eq. (1) and (2)) [33]. As was showed in Fig. S4. H_2O_2 species has a profound effect on catalytic

performance. In this case, decreasing the pH value would result in the high degradation efficiency.



Fig. S9 displayed the photocatalytic activity of the ternary composites prepared by changing the charging sequence with the mole fractions of graphene and Fe(III) fixed at 1% and 25%, together with that of 25%-Fe/CN. Interestingly, the photocatalytic activity of 25%-Fe/CN/GE was comparable to that of the 25%-Fe/CN sample that does not contain graphene, and lower than the 25%-CN/GE/Fe and 25%-Fe/GE/CN composites. It is suggested that the addition of graphene does not play a role in increasing the photocatalytic activity of 25%-Fe/CN/GE, revealing the absence of the synergistic effect between graphene and the Fe(III) species in this composite. Moreover, 25%-CN/GE/Fe, obtained from mixing g-C₃N₄ with graphene followed by adding the Fe(NO₃)₃ solution, almost exhibited the same photocatalytic activity as 25%-Fe/GE/CN, indicating that the similar synergistic effect between graphene and Fe (III) species existed in the two ternary composites. These results suggest the importance of the charging sequence for graphene. If the Fe(III) species first grafted on g-C₃N₄, then the addition of graphene probably has less influence on the photocatalytic activity of the obtained sample. It is implied that some of the Fe(III) species should be directly grafted on graphene.

Scheme 1 illustrated a tentative photocatalytic mechanism of the ternary 25%-Fe/GE/CN composite, together with that of the binary 25%-Fe/CN for comparison purpose. For the ternary photocatalyst (Scheme 1A), as IFCT is a surface phenomenon and the absorption electron number is not unlimited, the photo-excited electrons generated from g-C₃N₄ under visible light irradiation would be divided into two parts. One part could jump into the conduction band of g-C₃N₄ and combine with the dissolved O_2 to form $O_2^{\bullet-}$. With the aid of graphene, the electrons are able to quickly transfer to the surface to form active species and rapidly react with reactant which prior to absorb on graphene. And it needs to note that electrons in the CB of g-C₃N₄ (−1.23 V) cannot energetically transfer to Fe(III) (0.77 V), because of the large energy level difference and electrons in CB are prone to form $O_2^{\bullet-}$. Another part of the photo-generated electrons in the valence band of g-C₃N₄ are able to directly transfer to Fe(III) and form Fe(II) via the visible light initiate interfacial charge transfer (IFCT) ($Fe(III) + e^- = Fe(II)$, Fe^{3+}/Fe^{2+} , 0.771 V vs. SHE) [29a,35], while the holes still stay in the valence band of g-C₃N₄. It allows facilitating the rapid separation of photogenerated holes and electrons and shortening the electrons transmission distance, resulting in the enhancement in the mobility of holes and improving vis-

ible light absorption region. Notably, as Fe(II) is unstable and easily transforms into Fe(III) through the oxygen reduce under ambient condition, it means that Fe(III) would be recovered and Fe(III)/Fe(II) keeps dynamic equilibrium and the oxygen (O_2) turn into $O_2^{\bullet-}$ ($O_2 + Fe(II) + e^- = Fe(III) + O_2^{\bullet-}$, -0.046 V, vs. SHE) or H_2O_2 ($O_2 + Fe(II) + 2H^+ + 2e^- = Fe(III) + H_2O_2$, $+0.682$ V, vs. SHE) [22]. In this case, Fe(III)/Fe(II) species are capable of the multi-electron reduction of oxygen, when compared to the single electron reduction in CB of g-C₃N₄, enhancing the mobility of electrons and resulting in an increasing of photocatalytic activity. Furthermore, comparing the mild oxidant $O_2^{\bullet-}$ active species which just enable partial oxidation [33], holes in the VB of C₃N₄ show intensity photooxidation ability, revealing the good mineralization of MO or phenol. While, although hole is involved in photocatalytic reaction, just as demonstrated by the above discussion, it is not exclusively. So the photodegradation of MO is not completely transform into CO₂. Therefore, together with the above mentioned, the fast charge transfer enhance the separation of carriers, leaving hole in the VB of C₃N₄ and Fe(III) species allows the IFCT to yield more efficient electrons consumed for the reduction of oxygen process, thereby leading to the 25%-Fe/GE/CN composite presenting the best photocatalytic performance. Since the introduction of graphene results in the well distribution, small size and relatively high content of the Fe(III) species in the ternary composite, thereby leading to more active sites in the ternary composite than those in the binary one (Scheme 1B). Consequently, the higher optical absorption and the more reduced charge recombination were achieved by the ternary photocatalyst, leading to the better photocatalytic activity.

4. Conclusions

In summary, interfacial charge transfer effect (IFCT) was successfully introduced into g-C₃N₄ by grafting Fe(III) species on its surface via the impregnation method. The Fe(III)-grafted g-C₃N₄ showed enhanced photocatalytic activity which ascribed to the increasing visible-light sensitive and the reduced the recombination of photo induced carriers by the IFCT. When referred to the ternary Fe(III)/graphene/g-C₃N₄ photocatalyst, the introduction of graphene resulted in the well distribution, smaller size of the Fe species and the more efficient of the degradation activity among the prepared samples. This work demonstrated a facile way to obtain the transition metal embedded g-C₃N₄ based ternary photocatalysts which performed high photocatalytic activity via IFCT and without high temperature calcination process. It may provide a new opportunity to develop more highly efficient visible-light-driven photocatalysts for water disinfection.

Acknowledgement

This work was supported by the National Natural Science Foundation of China (No. 21276088 and 60976053)

Appendix A. Supplementary data

Supplementary data associated with this article can be found, in the online version, at <http://dx.doi.org/10.1016/j.apcatb.2015.10.054>.

References

- [1] F.E. Osterloh, Chem. Soc. Rev. 42 (2013) 2294–2320.
- [2] Y. Qu, X. Duan, Chem. Soc. Rev. 42 (2013) 2568–2580.
- [3] (a) X. Wang, K. Maeda, A. Thomas, K. Takanabe, G. Xin, J.M. Carlsson, K. Domen, M. Antonietti, Nat. Mater. 8 (2009) 76–80; (b) J. Zhang, X. Wang, Angew. Chem. Int. Ed. 54 (2015) 7230–7232.
- [4] (a) Y. Cui, Z. Ding, X. Fu, X. Wang, Angew. Chem. Int. Ed. 51 (2012) 11814–11818.
- [5] C. Han, L. Ge, C. Chen, Y. Li, X. Xiao, Y. Zhang, L. Guo, Appl. Catal. B-Environ. 147 (2014) 546–553.
- [6] (a) Z. Lin, X. Wang, Angew. Chem. Int. Ed. 52 (2013) 1735–1738.
- [7] Y. Hou, A.B. Laursen, J. Zhang, G. Zhang, Y. Zhu, X. Wang, S. Dahl, I. Chorkendorff, Angew. Chem. Int. Ed. Engl. 52 (2013) 3621–3625.
- [8] (a) J. Zhang, X. Chen, K. Takanabe, K. Maeda, K. Domen, J.D. Epping, X. Fu, M. Antonietti, X. Wang, Angew. Chem. Int. Ed. 49 (2010) 441–444.
- [9] (a) W. Zhao, Y. Guo, S.M. Wang, L.H. He, C. Sun, S.G. Yang, Appl. Catal. B-Environ. 165 (2015) 335–343.
- [10] (a) Y. Zheng, Y. Jiao, Y. Zhu, L.H. Li, Y. Han, Y. Chen, A. Du, M. Jaroniec, S.Z. Qiao, Nat. Commun. 5 (2014) 3783.
- [11] (a) X.-H. Li, X. Wang, M. Antonietti, Chem. Sci. 3 (2012) 2170–2174.
- [12] (a) P. Niu, L. Zhang, G. Liu, H.-M. Cheng, Adv. Funct. Mater. 22 (2012) 4763–4770.
- [13] (a) C. Creutz, B.S. Brunschwig, N. Sutin, J. Phys. Chem. B 109 (2005) 10251–10260.
- [14] (a) H. Irie, S. Miura, K. Kamiya, K. Hashimoto, Chem. Phys. Lett. 457 (2008) 202–205.
- [15] H. Yu, G. Cao, F. Chen, X. Wang, J. Yu, M. Lei, Appl. Catal. B: Environ. 160 (2014) 658–665.
- [16] X. Wang, X. Chen, A. Thomas, X. Fu, M. Antonietti, Adv. Mater. 21 (2009) 1609–1612.
- [17] (a) X. Ye, Y. Zheng, X. Wang, Chin. J. Chem. 32 (2014) 498–506.
- [18] (a) G. Zhang, C. Huang, X. Wang, Small 11 (2015) 1215–1221.
- [19] (a) S. Chowdhury, R. Balasubramanian, Appl. Catal. B: Environ. 160 (2014) 307–324.
- [20] Z. Chen, P. Sun, B. Fan, Z. Zhang, X. Fang, J. Phys. Chem. C 118 (2014) 7801–7807.
- [21] J. Ding, Q. Liu, Z. Zhang, X. Liu, J. Zhao, S. Cheng, B. Zong, W.-L. Dai, Appl. Catal. B: Environ. 165 (2015) 511–518.
- [22] H. Yu, H. Irie, Y. Shimodaira, Y. Hosogi, Y. Kuroda, M. Miyauchi, K. Hashimoto, J. Phys. Chem. C 114 (2010) 16481–16487.
- [23] T. Cui, R. Lv, Z.-H. Huang, H. Zhu, Y. Jia, S. Chen, K. Wang, D. Wu, F. Kang, Nanoscale Res. Lett. 7 (2012) 1–7.
- [24] H. Schmiere, J. Friebe, P. Streubel, R. Hesse, R. Köpsel, Carbon 37 (1999) 1965–1978.
- [25] Q. Liu, J. Zhang, Langmuir 29 (2013) 3821–3828.
- [26] J.F. Moulder, J. Chastain, R.C. King, Handbook of X-ray Photoelectron Spectroscopy: A Reference Book of Standard Spectra for Identification and Interpretation of XPS Data, Perkin-Elmer Eden Prairie, MN, 1992.
- [27] A.P. Grosvenor, B.A. Kobe, M.C. Biesinger, N.S. McIntyre, Surf. Interface Anal. 36 (2004) 1564–1574.
- [28] (a) Y. Zhu, S. Murali, W. Cai, X. Li, J.W. Suk, J.R. Potts, R.S. Ruoff, Adv. Mater. 22 (2010) 3906–3924.
- [29] (a) M. Liu, X. Qiu, M. Miyauchi, K. Hashimoto, J. Am. Chem. Soc. 135 (2013) 10064–10072.
- [30] A.J. Bard, R. Parsons, J. Jordan, Standard Potentials in Aqueous Solution, CRC press, 1985.
- [31] (a) T. Chen, Y. Zheng, J.-M. Lin, G. Chen, J. Am. Soc. Mass Spectrom. 19 (2008) 997–1003.
- [32] Z. Chen, W. Wang, Z. Zhang, X. Fang, J. Phys. Chem. C 117 (2013) 19346–19352.
- [33] Y. Cui, Z. Ding, P. Liu, M. Antonietti, X. Fu, X. Wang, Phys. Chem. Chem. Phys. 14 (2012) 1455–1462.
- [34] W. He, H. Jia, W.G. Wamer, Z. Zheng, P. Li, J.H. Callahan, J.-J. Yin, J. Catal. 320 (2014) 97–105.
- [35] M. Nishikawa, Y. Mitani, Y. Nosaka, J. Phys. Chem. C 116 (2012) 14900–14907.